Author/s:
Liu, Z;Wang, X;Guo, R;Richardson, JJ;Wang, T;Xu, W;Caruso, F;Pan, S

Title:
Highly Stable and Active Flexible Electrocatalysts Derived from Lotus Fibers

Date:
2023-03-23

Citation:
Liu, Z., Wang, X., Guo, R., Richardson, J. J., Wang, T., Xu, W., Caruso, F. & Pan, S. (2023). Highly Stable and Active Flexible Electrocatalysts Derived from Lotus Fibers. Advanced Functional Materials, 33 (13), https://doi.org/10.1002/adfm.202211563.

Persistent Link:
https://hdl.handle.net/11343/326010

Spray Coating Experiments: Setups and Methodologies

The latest eBook from Advanced Optical Metrology. Download for free.

Spray Coating Experiments: Setups and Methodologies, is the third in our Thin Films eBook series. This publication provides an introduction to spray coating, three article digests from Wiley Online Library and the latest news about Evident's Image of the Year Award 2022.

Wiley in collaboration with Evident, are committed to bridging the gap between fundamental research and industrial applications in the field of optical metrology. We strive to do this by collecting and organizing existing information, making it more accessible and useful for researchers and practitioners alike.

EVIDENT
OLYMPUS

WILEY

ADVANCED FUNCTIONAL MATERIALS
www.afm-journal.de

Highly Stable and Active Flexible Electrocatalysts Derived from Lotus Fibers

Zhen Liu, Xuxu Wang, Rui Guo, Joseph J. Richardson, Tianzheng Wang, Weijian Xu, Frank Caruso, and Shuaijun Pan**

The stability and activity of electrocatalysts are fundamental in energy-related applications (e.g., hydrogen generation and energy storage). Electrocatalysts degrade over time when the active centers are not strongly anchored to the support. However, if the active centers are too strongly anchored, the activity of the electrocatalysts decreases due to reduced accessibility to reactants. Herein, a strategy is presented to balance the stability and activity of different active materials using a natural and flexible support material that can be woven and carbonized. Lotus fibers, which have surface hydroxyl and phenolic groups, high mechanical strength, and a mesoscale porosity post-pyrolysis, are used to load diverse functional metal-containing materials such as metal–organic frameworks, 2D materials, metal sulfide nanoparticles, metal ions, and high-entropy alloys. After pyrolysis, the electrocatalysts display flexibility, high catalytic performance, and long-term stability, outperforming commercial benchmarks (e.g., Pt/C) in specific scenarios for water splitting, liquid batteries, and flexible electronics.

1. Introduction

Functional materials have a wide range of applications in diverse fields such as high-strength fibers,[1,2] flexible wearables,[3,4] sensing,[5] bioengineering,[6] and batteries and catalysis.[7,8] Specifically, advanced catalytic materials show promise for addressing the global energy crisis owing to their extensive use in energy conversion and storage systems such as fuel cells,[9] water splitting,[10] and metal-ion batteries.[11] The design of high-performance catalysts typically involves the engineering of catalytic centers (e.g., nanoparticles (NPs), alloys) followed by their binding to either support materials or the working electrode, with the aim of balancing long-term stability with high catalytic performance.[12] Adhesive bonding often suffers from the degradation of electrocatalysts during long-term anodic or cathodic reactions and therefore their stability is an ongoing issue.[13,14] Strong metal–support interactions[15] (SMSIs) offer a solution for stabilizing the electrocatalytic centers onto support materials; however, this can reduce their catalytic activity, as the strong bonding can lead to a hindered access to the catalytic centers.[16] Therefore, the engineering of high-performance electrocatalysts requires the rational selection of support materials that can maintain strong interactions without blocking the active centers.[17–20]

Suitable supports not only stabilize dispersed catalytic active centers, but also can control the particle morphology and electronic structure through SMSIs, thereby promoting the performance of the catalyst.[12,21] Conventional carbon-based supports,[22–25] including carbon nanotubes (CNTs),[26] graphene,[27] electrospun fibers,[28] and carbon nitrides,[29] are often used owing to their high conductivity. However, these materials have few reducible anchoring groups for the catalytic centers (i.e., weak interfacial interactions) and often are costly, and/or involve complicated, toxic, and energy- and time-intensive preparation procedures. MXene is a class of 2D metal carbides[30–32] that display metallic conductivity and feature hydroxyl groups or terminal oxygen on their surface

Z. Liu, X. Wang, R. Guo, W. Xu, S. Pan
State Key Laboratory of Chemo/Biosensing and Chemometrics, and College of Chemistry and Chemical Engineering
Hunan University
Changsha 410082, China
E-mail: pansj@hnu.edu.cn

X. Wang
College of Environmental Science and Engineering
Hunan University
Changsha 410082, China

The ORCID identification number(s) for the author(s) of this article can be found under https://doi.org/10.1002/adfm.202211563.

DOI: 10.1002/adfm.202211563

R. Guo, J. J. Richardson, T. Wang, F. Caruso, S. Pan
Department of Chemical Engineering
The University of Melbourne
Parkville, Victoria 3010, Australia
E-mail: fcaruso@unimelb.edu.au

R. Guo
College of Chemistry and Materials Science
Hunan Agricultural University
Changsha 410128, China

J. J. Richardson
Department of Materials Engineering
The University of Tokyo
7-3-1 Hongo, Bunkyo, Tokyo 113-8656, Japan

J. J. Richardson
School of Engineering
RMIT University
Melbourne, Victoria 3000, Australia

for anchoring purposes. However, the use of MXene typically requires pre- or post-treatments (e.g., the use of hydrofluoric acid). In this regard, naturally abundant biomass (e.g., silk, plant fibers) that are rich in reducible functional anchoring groups (i.e., strong interfacial interactions) are promising alternatives for the development of next-generation advanced catalysts.[7,33] Moreover, biomass is typically a soft material that would be suitable for producing flexible and weavable catalytic materials.

Herein, we explore loading, stabilizing, and activating nanomaterials using naturally abundant and flexible lotus fibers (LFs). LFs are flexible and weavable fibers high in toughness[34] and rich in hydroxy, phenol, and/or amino groups, generally consisting of cellulose and lignin with various other water-soluble and insoluble components.[35] These functional groups can robustly anchor catalytically active metal centers and/or nanomaterials, such as metal–organic frameworks (MOFs) (e.g., zeolitic imidazolate framework-67), 2D materials (e.g., molybdenum disulfide), metal sulfide NPs (i.e., cobalt sulfide Co_9S_8 NPs), and other metal precursors (Mn^{2+}, Fe^{3+}, Co^{2+}, Ni^{2+}, and Cu^{2+}). Upon pyrolysis,[36] LFs can be rendered conductive and retain their flexibility, which enables the conversion of the pre-loaded precursors into stabilized and advanced catalytic materials through SMSIs and/or space confinement within the mesoporous carbonized matrix, such as high-entropy alloys (e.g., quinary Mn-Fe-Co-Ni-Cu alloys) and heteroatom-doped catalysts (e.g., nitrogen- and sulfur-doped carbon loaded with Co_9S_8 NPs, namely Co_9S_8-NSC). It is noted that Co_9S_8 is a class of promising electrocatalysts[37] featuring rich redox chemistry (i.e., multi-valence cobalt active centers), high electron conductivity, good stability (both mechanical and thermal), as well as desirable tolerance to oxygen (oxidation resistance). Therefore, Co_9S_8-based catalysts are selected to better discuss the main findings with a focus on using highly flexible lotus fibers as the support in this work. Both current experimental and computational studies reveal that the engineered flexible electrocatalysts using Co_9S_8-NSC can perform three electrochemical functions that is hydrogen evolution reaction (HER), oxygen evolution reaction (OER), and oxygen reduction reaction (ORR). The triple functionality makes Co_9S_8-NSC a suitable cathode material for liquid zinc-air batteries (ZABs), which in turn can further power the electrolysis of water (i.e., water splitting) where the catalysts are deployed as both cathode and anode materials. In addition, the flexibility and weavability of the engineered catalysts allow for their application in flexible solid-state ZABs and wearable electronics. In addition to the focus on the engineering of flexible catalysts that are both active and stable at relevant electrochemical processes, this work provides a strategy for engineering advanced functional composite materials for future energy-related applications and paves a way for additive manufacturing using nanomaterials.

2. Results and Discussion

2.1. LFs

LFs are long fibers extracted from lotus root, which exhibit a hierarchical morphology of helical bundles of elementary cellulose fibers composed of 4–8 fibrils each consisting of parallel-stacked cellulose and hemicellulose chains[35] (**Figure 1**a; Figure S1, Supporting Information). The helical fibers have good elasticity and tensile strength and have been known as a high-quality weavable material, thus they are expected to be a suitable support material for the rational design of flexible electrocatalysts with high mechanical strength (i.e., stability). We found that carbon, oxygen, and nitrogen are dominant in LFs, taking up > 98.3 at.% (Figure S2, Supporting Information). Fourier transform infrared spectroscopy suggests the existence of hydroxy or amino groups at ≈3440 cm^{-1}, aliphatic hydrocarbons at ≈2890 cm^{-1}, benzene skeleton in lignin at ≈1630 cm^{-1}, uronic ester bridges in hemicellulose at ≈1160 cm^{-1}, ether linkages between glucose units at ≈1060 cm^{-1}, and β-glycoside bonds in cellulose at ≈890 cm^{-1} (Figure S3a, Supporting Information).[38] These abundant reducible groups (such as hydroxy groups) can potentially facilitate chemical modifications and the loading of catalytically active centers, and the elimination of volatile species (e.g., oxygen-containing groups) at high temperatures upon pyrolysis may contribute to generating a large number of mesopores (Figure S3b, Supporting Information). Specifically, the oxygen-containing functional groups are conducive to homogeneous anchoring of cations and nanomaterials, and the nanoporous characteristics are important for efficient mass transfer and/or the exposure of anchored active species in the catalyst system (i.e., sustained activity and enhanced stability).

2.2. Nanomaterials Incorporated into LFs

The hydroxy and/or amino groups of LFs can interact with metal ions (e.g., Mn^{2+}, Fe^{3+}, Co^{2+}, Ni^{2+}, and Cu^{2+}) through electrostatic interactions, and the complex can serve as the precursors for diverse nanomaterials. For example, MOFs such as zeolitic imidazolate framework-67 were uniformly loaded onto the surface of LFs by simply mixing the precursors (i.e., Co^{2+} and 2-methylimidazole) with LFs, followed by incubation at room temperature (≈25 °C) for 24 h (Figure S4, Supporting Information), similar to previous studies using zeolitic imidazolate framework 8 in living plants.[39] Alternatively, hydrothermal processes could be applied to generate 2D materials such as molybdenum disulfide[40] (MoS_2; Figure S5, Supporting Information). In addition, metal sulfide NPs[41] (e.g., cobalt sulfide Co_9S_8) were grown on LFs simply by mixing cobalt(II) nitrate hexahydrate with thiourea at ≈25 °C for 2 h, followed by a hydrothermal step at 180 °C for 24 h (Figure S6, Supporting Information). Upon pyrolysis at 900 °C, LFs largely maintained their fibrous features, flexibility, and mechanical strength, with a structural transformation yielding porous surface features (Figure S7, Supporting Information) due to the breaking of chemical bonds and evaporation of water during heating.[35] In contrast, Co_9S_8 NPs loaded on a commercial carbon support, Vulcan XC 72R, were loosely stacked and aggregated with a low surface coverage and poor stability (Figure S8, Supporting Information), further highlighting the importance of strong interfacial interactions. The nanoporous structure of pLF also contributed to a balanced high activity and stability (i.e., high exposure of strongly anchored active metal centers). Of note, a single pyrolyzed lotus fiber (pLF; ≈1–2 μm in diameter) can bear a weight of > 25 mg (i.e., > 1000 times its own weight) (Figure 1b,c). High-entropy Mn-Fe-Co-Ni-Cu alloys with an average diameter of ≈60 nm could also be obtained by

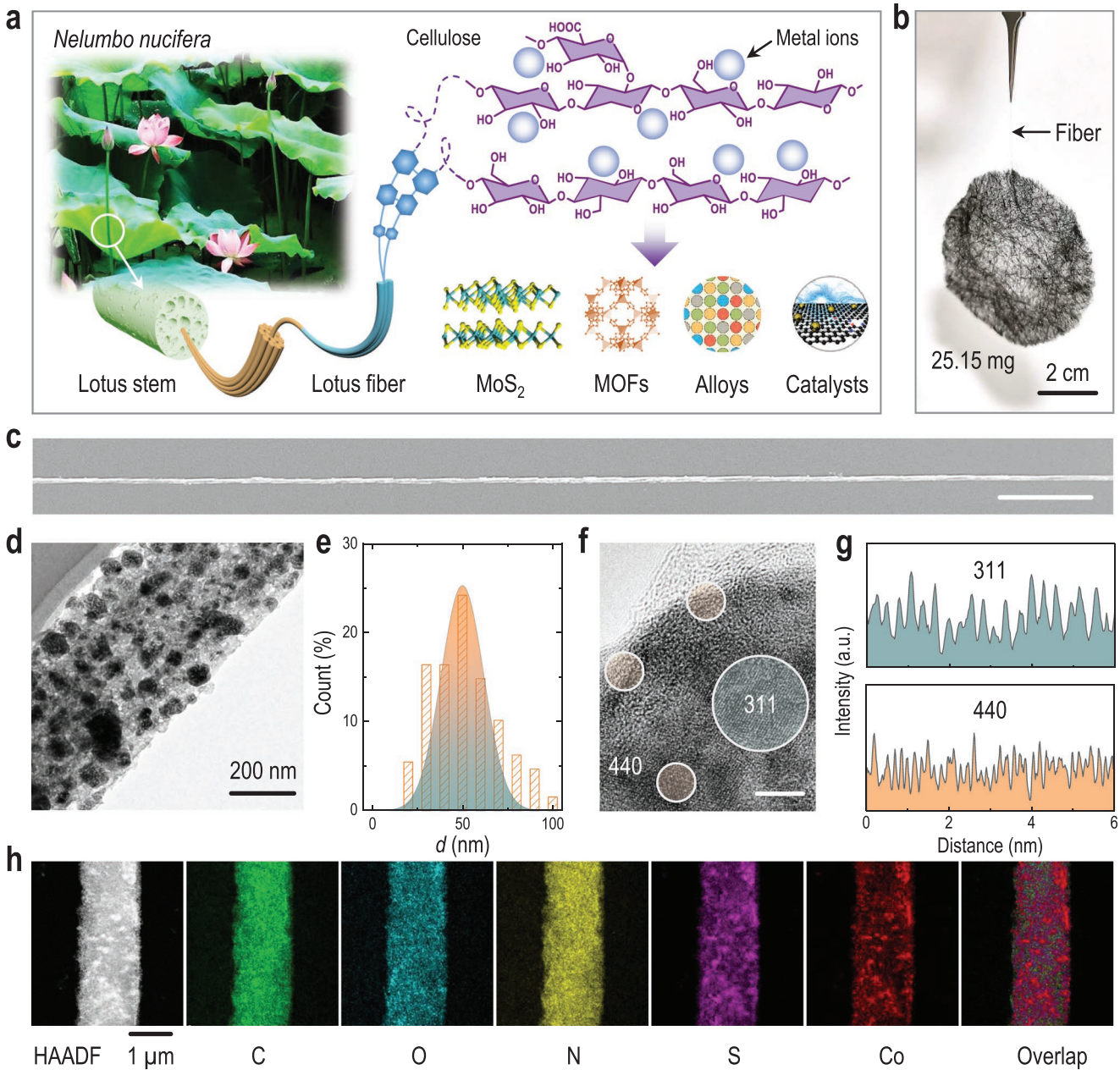

Figure 1. Nature-inspired loading of nanomaterials using LFs. a) Hierarchical structure of LFs, interactions with metal ions, and the loading of MoS_2, MOFs, alloys, or catalysts. b) Pyrolyzed lotus fabric mat held by a single fiber. c) Scanning electron microscopy image of the fiber (in b) isolated from the pyrolyzed woven mat. Scale bar is 200 µm. d) TEM image of the flexible catalyst (Co_9S_8-NSC). e) Size Gaussian normal distribution of the loaded Co_9S_8 NPs. The sample size is > 150 NPs. f) HR-TEM image of Co_9S_8-NSC. Scale bar is 5 nm. g) Lattice profiles of the crystalline regions identified in f). h) HAADF-STEM image and corresponding element mappings of Co_9S_8-NSC.

pyrolyzing their quinary metal ion precursors pre-loaded on LFs (Figure S9, Supporting Information). When pyrolyzing the Co_9S_8-loaded LFs, the aggregated Co_9S_8 NPs transformed into uniformly confined and individual NPs (Figure 1d; Figure S10, Supporting Information) with an average diameter of ≈50 nm (Figure 1e). This suggests that the carbon matrix of LFs has a good anchoring capability and can prevent aggregation—a critical factor for catalytic reactions. It is noted that the loading of these nanomaterials is robust and independent of the season that the LFs are obtained (Figure S11, Supporting Information).

2.3. Structural Characterization of the Pyrolyzed Catalysts

Transmission electron microscopy (TEM) revealed that the Co_9S_8 NPs were partially encapsulated by a porous carbon layer (Figure S12, Supporting Information) due to the SMSI effect that contributes to the stability of the catalyst.[16,42] The samples displayed two types of inter-lattice spacing (i.e., 0.30 and 0.18 nm) of the crystalline regions under high-resolution TEM (HR-TEM), demonstrating the presence of the (311) and (440) planes of the Co_9S_8 nanocrystals, respectively (Figure 1f,g).

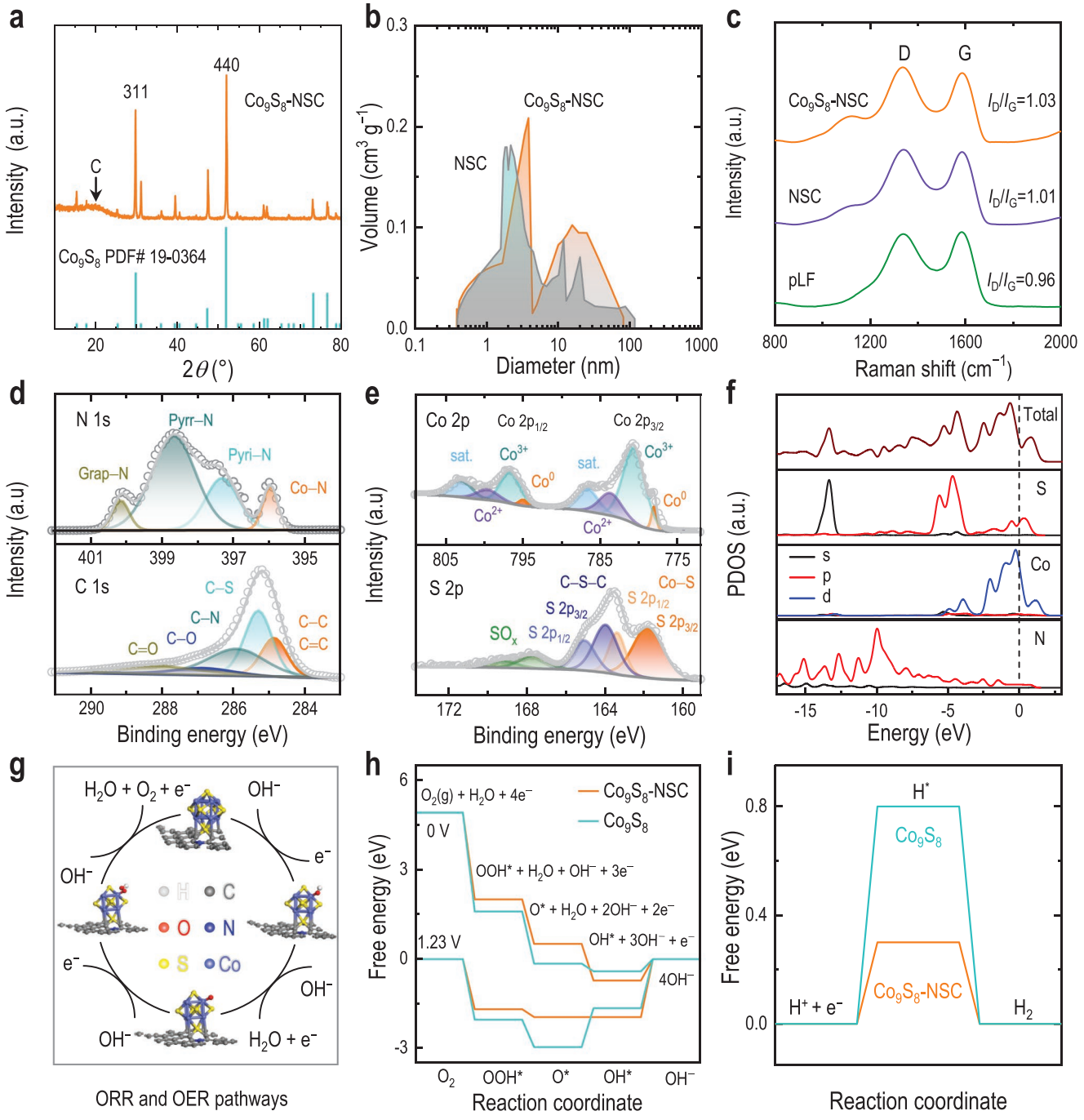

Figure 2. Structural and theoretical analysis. a) XRD patterns of Co_9S_8-NSC. The reference XRD pattern for Co_9S_8 is also shown. b) Pore size distributions of Co_9S_8-NSC and NSC, as assessed by N_2 adsorption/desorption. c) Raman spectra of Co_9S_8-NSC, NSC, and pLF. d,e) N 1s and C 1s d) and Co 2p and S 2p e) HR-XPS spectra of Co_9S_8-NSC. f) Calculated PDOSs of Co_9S_8-NSC. g) OER and ORR mechanisms. h) Calculated free energy diagrams and reaction pathways of ORR at different applied voltages. i) Calculated free energy diagram of the HER process.

High-angle annular dark field scanning transmission electron microscopy (HAADF-STEM) and elemental mapping indicated that carbon, oxygen, nitrogen, and sulfur coexist with relatively uniform coverage in the pyrolyzed catalyst containing Co_9S_8 NPs (i.e., Co_9S_8-NSC) (Figure 1h). X-ray diffraction (XRD) and small-angle X-ray scattering of Co_9S_8-NSC further confirmed that the composition was mixed between amorphous carbon and Co_9S_8 nanocrystals (**Figure 2**a; Figure S13, Supporting Information).[43] The N_2 adsorption/desorption isotherms of Co_9S_8-NSC displayed a Type IV isotherm, with an adsorption hysteresis observed at relative pressure 0.4–1.0 that was indicative of the existence of a mesoporous structure (Figure S14a, Supporting Information), which would be beneficial for mass transfer during electrocatalysis. The introduction of Co_9S_8

NPs could generate more structural defects (e.g., mesopores; Figure 2b) in contrast to the control samples (i.e., pyrolyzed LFs doped with nitrogen and sulfur, namely NSC). Raman spectra of Co_9S_8-NSC further suggested the slightly increased defects of the graphitic substrate by the increased ratios between the *D* band (1327 cm^{-1}) and the *G* band (1571 cm^{-1}) (Figure 2c). This is likely due to the locally high temperature and thus increased evaporation of the carbon support in the doped samples upon pyrolysis. Notably, increased graphitic defects are conducive to enhanced access to catalytic active sites.[44]

2.4. Chemical Characterization of Co_9S_8-NSC

The heteroatom-doped electrocatalyst (i.e., Co_9S_8-NSC) was further examined by high-resolution X-ray photon spectroscopy (HR-XPS) (Figure 2d,e; Figure S14b, Supporting Information), where the spectra of carbon, nitrogen, cobalt, and sulfur revealed the bonding structure of the hybrid catalyst. The high-resolution C 1s spectrum showed deconvolved peaks at 284.8 and 285.3 eV corresponding to the sp^2- and sp^3-hybridized C—C and C—S bonds,[45] respectively (Figure 2d). The peaks located at 286.1, 286.9, and 288.6 eV correspond to C—N, C—O, and C=O bonds, respectively.[46] The metallic N (e.g., Co—N; 396.0 eV) and the graphitic N (i.e., grap–N; 400.2 eV) in the catalyst can improve electron transfer and proton adsorption,[47] while the pyrrolic N (i.e., pyrr–N; 398.6 eV) and the pyridinic N (i.e., pyri–N; 397.3 eV) can increase the hydrophilicity of the catalyst and the local contact area between the catalyst and the electrolyte solution, thereby promoting proton transfer[48] (Figure 2d). The S 2p HR-XPS spectrum indicated three possible chemical environments: doped S in pLF (i.e., S—C; 164.0 and 165.1 eV), metallic S in Co_9S_8 NPs (i.e., Co—S; 161.9 and 163.4 eV), and oxidized S due to oxygen adsorption (e.g., SO_x; 167.7 and 169.4 eV) on the Co_9S_8 active surface[49] (Figure 2e). The fitted Co 2p spectrum suggested the presence of three valency states: Co^{3+} (780.9 and 796.8 eV), Co^{2+} (783.9 and 799.8 eV), and Co^0 (778.1 and 795.1 eV)[50] (Figure 2e). In addition, HR-XPS of O 1 s revealed the presence of oxygen in four different states in the sample: adsorbed oxygen or Co—O (529.5 eV), C=O (531.1 eV), H—O—C (532.0 eV), and O=C—O (533.5 eV) (Figure S14c, Supporting Information).[51] This result suggests that the oxygen residue is present due to the partial elimination of reducible groups in LFs during pyrolysis and can possibly/partially serve as the anchor site (though not dominant) for Co_9S_8 NPs based on the XPS peak fitting at ≈529.5 eV (e.g., metal oxides). However, further SEM examination of samples obtained in the presence or absence of sulfur doping suggests that sulfur may play a more significant role in anchoring Co_9S_8 NPs (Figure S8 and S15, Supporting Information).

2.5. Theoretical Analysis of Co_9S_8-NSC

We further evaluated the Co_9S_8 and Co_9S_8-NSC systems at the atomic and molecular scales using density functional theory (DFT) calculations. The doped model was constructed by doping both nitrogen and sulfur in the carbon support (i.e., pLF) with the doped sulfur serving as the anchor site for Co_9S_8 NPs according to the literature[52–54] and our experimental and theoretical findings (Figure S8, S15, and S16 and Table S1, Supporting Information). Specifically, control samples without sulfur doping displayed poor loading and pronounced aggregation of Co_9S_8 NPs (Figure S8 and S15, Supporting Information), which was consistent with the findings of the anti-sintering effect of sulfur on metal NPs reported in the literature.[53,54] DFT models using either nitrogen or oxygen as the anchor site revealed that the binding energies of Co—N and Co—O were –0.18 eV and –1.11 eV, respectively, which were much weaker than that of Co—S (–2.09 eV) (Figure S16 and Table S1, Supporting Information). These results collectively suggest that using sulfur as the anchor site in this work is energetically preferred, experimentally relevant, and theoretically representative, although other anchoring pathways (e.g., physical adsorption, space confinement, and chemical anchoring with diverse heteroatoms) cannot be ruled out. When using sulfur as the anchor (proposed pathway in this work), the projected density of state (PDOS) analysis showed an overlap of the s- and p-orbitals of Co with that of S (and N) in the nitrogen-doped system, indicating strong covalent interactions between Co and S (and N) upon nitrogen doping (Figure 2f; Figure S17, Supporting Information), as also evidenced by the XPS results. Of note, the anchoring of Co_9S_8 NPs onto the N- and S-doped carbon support increases the d orbital energy of Co (by d–p coupling between Co and N atoms), moving the antibonding state upward above the Fermi level, resulting in a reduced filling of electrons in the antibonding state. This is essential for interfacial adsorption/reactions. Therefore, the interfacial adsorption/reaction processes of free Co_9S_8 NPs and Co_9S_8-NSC system were also evaluated to provide insight for possible electrochemical processes (e.g., OER and ORR) (Figure 2g; Figure S18, Supporting Information). The Gibbs free energy of the adsorption of all the intermediate species (including OOH*, O*, and OH*) was downhill for Co_9S_8-NSC at the oxidation and reduction potential of oxygen (0 and 1.23 V), indicating that the ORR can proceed spontaneously except for the rate-determining step where OH* is converted into hydroxy groups (Figure 2h). A similar trend was observed for the non-doped Co_9S_8 NPs at 0 V, whereas at 1.23 V the active sites could be covered by O* resulting in the increased adsorption of OH*, thereby decreasing ORR performance. That is, upon S and N doping and the loading of Co_9S_8 NPs into pLF, the adsorption of O* and OH* can be balanced, suggesting the synergistic effect between Co_9S_8 and NSC[52,55] and facilitating possible ORR and OER (i.e., reverse process of ORR) applications. In addition, the Gibbs free energy for hydrogen adsorption was calculated to evaluate the possible HER activity (Figure 2i; Figure S19, Supporting Information). The computed H* adsorption energy of Co_9S_8-NSC was reduced by > 60% relative to that of Co_9S_8 NPs, indicating the preferred hydrogen binding (i.e., improved H*-chemisorption properties for efficient HER).

2.6. Triple Electrochemical Functions of Co_9S_8-NSC

A strong cathodic peak at 0.86 V was observed in the cyclic voltammetry curve of the engineered Co_9S_8-NSC when measured in O_2- saturated 0.1 M KOH electrolyte (Figure S20a,

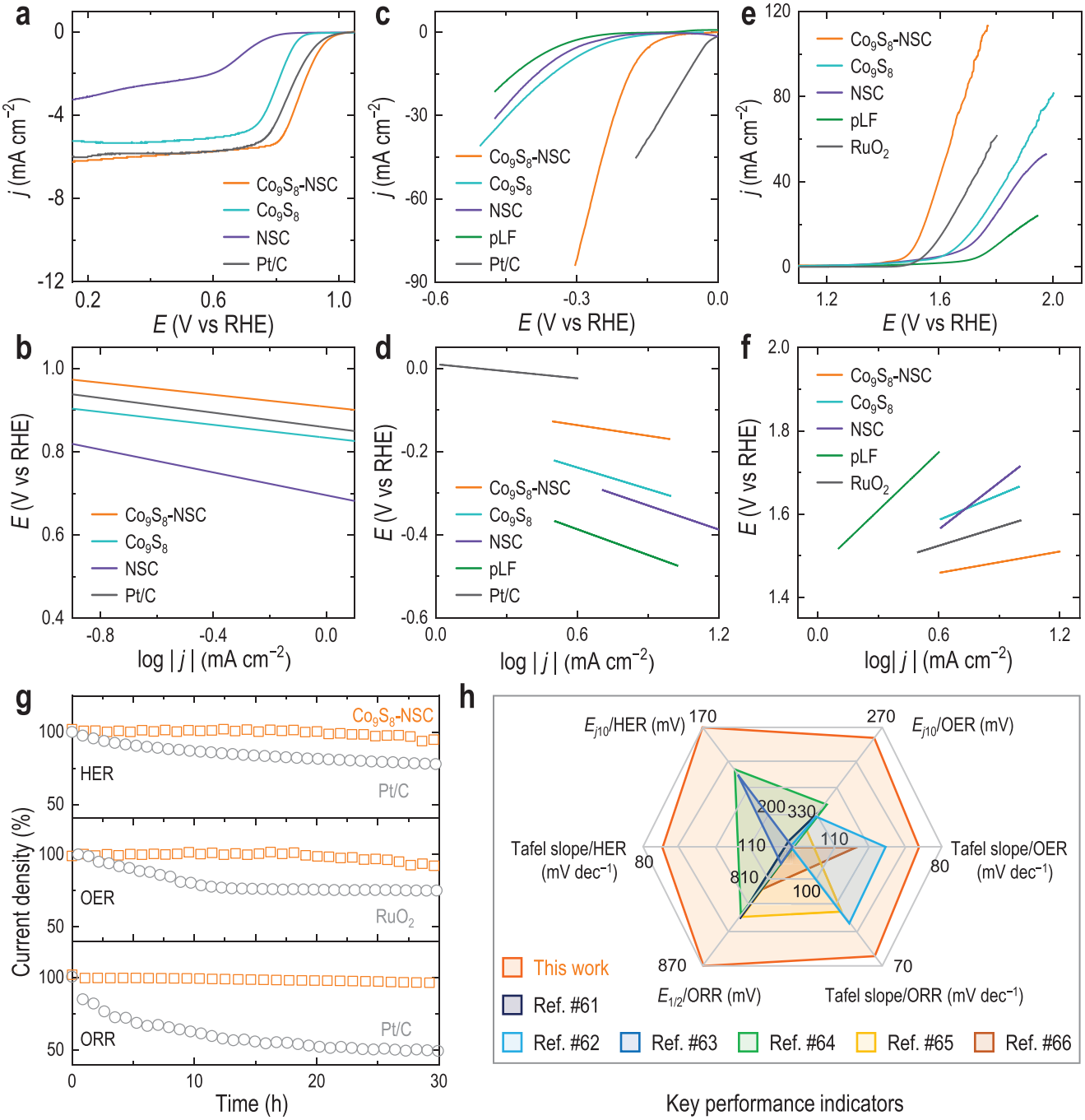

Figure 3. Electrocatalytic functions. a,b) ORR polarization curves a) and Tafel plots derived from ORR polarization curves b) of different catalysts. The electrolyte is O_2-saturated 0.1 M KOH. c,d) HER polarization curves c) and Tafel plots derived from HER polarization curves d) of different catalysts. e,f) OER polarization curves e) and Tafel plots derived from OER polarization curves f) of different catalysts. The electrolyte used in the HER and OER processes is 1 M KOH. g) Electrocatalytic stability of Co_9S_8-NSC and commercial catalysts Pt/C and RuO_2 in HER, OER, and ORR processes. The applied voltages are the corresponding overpotentials determined at 10 mA cm^{-2}. h) Comparison of the electrocatalytic performance of Co_9S_8-NSC and state-of-the-art cobalt-based catalysts (shaded area).

Supporting Information), suggesting its potential in ORR. Linear scan voltammogram (LSV) curves demonstrated that Co_9S_8-NSC exhibited the highest onset potential at a current density of 0.01 mA cm^{-2} (≈1.03 V; Figure S20b, Supporting Information) and half-wave potential (0.87 V) (**Figure 3**a) of all the samples studied. Moreover, the half-wave potential of Co_9S_8-NSC is higher than that of most non-noble metal ORR catalysts reported in the literature (Table S2, Supporting Information). Co_9S_8-NSC also displayed faster ORR kinetics as evidenced by the smaller calculated Tafel slope (72.5 mV dec^{-1}) compared with that of a commercial Pt/C catalyst (83.4 mV dec^{-1}) (Figure 3b). Koutecky-Levich (K-L) plots were calculated using the LSV curves obtained at different rotation speeds, and the linearity indicated first-order reaction kinetics (as a function of

dissolved O_2) (Figure S20c, Supporting Information). A 4-electron path[51] was determined by the slope of these K-L plots (i.e., ≈3.9) for the relevant ORR process (i.e., reduction of O_2 into H_2O instead of H_2O_2). The selective reduction of O_2 was also studied using a rotating ring disk electrode, where the smaller loop current density of the Co_9S_8-NSC suggested a slower production of H_2O_2 (i.e., < 3%), and the number of transferred electrons was confirmed as 3.9 at low potentials (0.2–0.8 V) (Figure S20d,e, Supporting Information). We also note that the Co_9S_8-NSC was tolerant to methanol (Figure S20f, Supporting Information), indicating its potential use in fuel cell applications in conjunction with the highly selective 4-electron pathway as mentioned above.[46]

Next, the HER performance of Co_9S_8-NSC was evaluated using 1 M KOH as the electrolyte. The composite Co_9S_8-NSC afforded a much lower overpotential (172 mV at –10 mA cm^{-2}) compared to the controls (e.g., 315 mV for the non-loaded Co_9S_8 NPs) (Figure 3c), suggesting its higher HER activity, which is also better than that of reported cobalt-based HER catalysts in the literature (Table S3, Supporting Information). The fitted Tafel slope of Co_9S_8-NSC was 85.0 mV dec^{-1}, suggesting that its rate-determining step was the Heyrovsky step (i.e., $H^* + H^+ + e^- \rightarrow H_{2+*}$), whereas that of the control samples was the Volmer step (i.e., $H^+ + e^- + * \rightarrow H^*$) considering their higher Tafel slopes of > 120 mV dec^{-1} (i.e., higher adsorption energy, $|\Delta G_{H^*}|$)[56] (where * denotes an active site on the electrode surface) (Figure 3d). In addition, the double-layer capacitance (C_{dl}) was determined based on the potential range of the non-Faradaic process. The C_{dl} values of all the catalysts decreased in the order of Co_9S_8-NSC > Co_9S_8 > NSC > pLF, suggesting that Co_9S_8-NSC displayed the highest electrochemically active surface area (ECSA) among all catalysts[57] (Figure S21, Supporting Information). Furthermore, the charge transfer resistance (R_{ct} = 5.4 Ω) between Co_9S_8-NSC and electrode surface was much lower than that involving the control catalysts (Figure S22, Supporting Information), which can be attributed to the better conductivity rendered by the pLF support.[58] The OER activity of composite Co_9S_8-NSC was also high, as indicated by the low OER overpotential (276 mV at –10 mA cm^{-2}; Figure 3e), the low Tafel slope (85.5 mV dec^{-1}; Figure 3f), the high C_{dl} value (12.8 mF cm^{-2}; Figure S23a, Supporting Information), the large ECSA value (320; Figure S23b, Supporting Information), the small R_{ct} value (9.3 Ω; Figure S23c, Supporting Information), and the high turnover frequency (e.g., 2.27 s^{-1} at an overpotential of 300 mV; Figure S24, Supporting Information) compared to the controls (e.g., Co_9S_8 NPs, NSC, and pLF) and those reported in the literature (Table S4, Supporting Information).

In addition, Co_9S_8-NSC displayed long-term ORR, HER, and OER durability (i.e., negligible change in current densities over 30 h) when compared to commercial noble metal catalysts (e.g., Pt/C and RuO_2) (Figure 3g). It is noted that the OER test involves a harsh condition (i.e., high anodic potential); however, our catalyst displayed no apparent changes in the phase and structure (e.g., no CoOOH species found) after OER (276 mV for 30 h), indicating the high stability of the catalyst (Figure S25–S27, Supporting Information). In addition, we examined the XPS spectra of Co_9S_8-NSC after OER test at 276 mV for 30 h (Figure S28, Supporting Information). The binding energies and relative intensities of Co 2p were unchanged, suggesting the stability of the loaded Co_9S_8 NPs (Figure S28a, Supporting Information). The binding energies of S 2p in Co_9S_8 were also largely unchanged (163.4 eV) with more Co—S bonds observed at 161. 9 eV. However, excess S (owing to doping) possibly oxidized to more SO_x (169.4 eV) (Figure S28b, Supporting Information). The relatively low intensity of Co—N bonding at 396.0 eV before the OER test decreased further after the OER test, indicating the weak interaction between nitrogen and cobalt (Figure S28c, Supporting Information). The chemical states of carbon matrix and oxygen were largely unchanged (Figure S28d,e, Supporting Information). Of note, the decrease of Co—N bond and increase of Co—S bond after the OER test collectively suggest that cobalt and sulfur display a strong interaction (i.e., energetically preferred anchoring of cobalt by sulfur), as consistent with the DFT calculations (Figure S16, Supporting Information). In addition to revealing the stability of our catalyst system, the XPS experiments suggest that the binding of cobalt could be complicated, whereas sulfur binding is likely dominant both before and after the OER test. Therefore, the high stability possibly originates from the strong interactions between the catalytic centers (Co_9S_8 NPs) and the sulfur-doped carbon matrix (pLF). The porous pLF can not only confine the Co_9S_8 NPs in a 3D configuration within the network, thus preventing their aggregation, but also protects the catalytic centers from deactivation by forming a thin layer on the exposed Co_9S_8 NPs. The superior ORR/HER/OER performance of Co_9S_8-NSC can be attributed to the following factors: i) abundant mesopores of LFs upon pyrolysis (i.e., enhanced mass transfer[59]); ii) increased exposure of active sites (i.e., nanoporous structure upon pyrolysis); iii) significantly increased conductivity after pyrolysis of the biomass (i.e., good for electron transfer); iv) optimized electronic structure of the catalytically active Co_9S_8 NPs after N and S doping (i.e., reduced free energy of catalytic processes); and v) SMSIs and synergistic effects[60] achieved by chemically embedding the Co_9S_8 NPs into the conductive and micro/mesoporous pLF. Overall, nanoengineered Co_9S_8-NSC exhibited low overpotentials (E_{j10}) at a current density (j) of 10 mA cm^{-2} for HER and OER, a high half-wave potential ($E_{1/2}$) for ORR, and low Tafel slopes for ORR, HER, and OER in contrast to recently reported electrocatalysts[61–66] (Figure 3h). These improved performances suggest that Co_9S_8-NSC has promise in rechargeable ZABs (i.e., ORR and OER) and water splitting (i.e., HER and OER).

2.7. Co_9S_8-NSC-Based Liquid ZABs

We assembled liquid ZABs using Co_9S_8-NSC or commercial Pt/C catalyst (i.e., control sample) as the air-cathode catalysts (**Figure 4**a) and found that Co_9S_8-NSC could help maintain a higher open-circuit voltage (1.49 V for over 12 h) than the commercial counterpart (Figure 4b). The discharge voltages were high and stable at different current densities (2–30 mA cm^{-2}) and were fully restored when the current density was set to the initial value (Figure S29a, Supporting Information), indicating the good rate performance and restorability of Co_9S_8-NSC. The maximum output power density of Co_9S_8-NSC could reach 141 mW cm^{-2}, outperforming the Pt/C control (112 mW cm^{-2}) in a wide range of current densities (0–500 mA cm^{-2}) (Figure 4c).

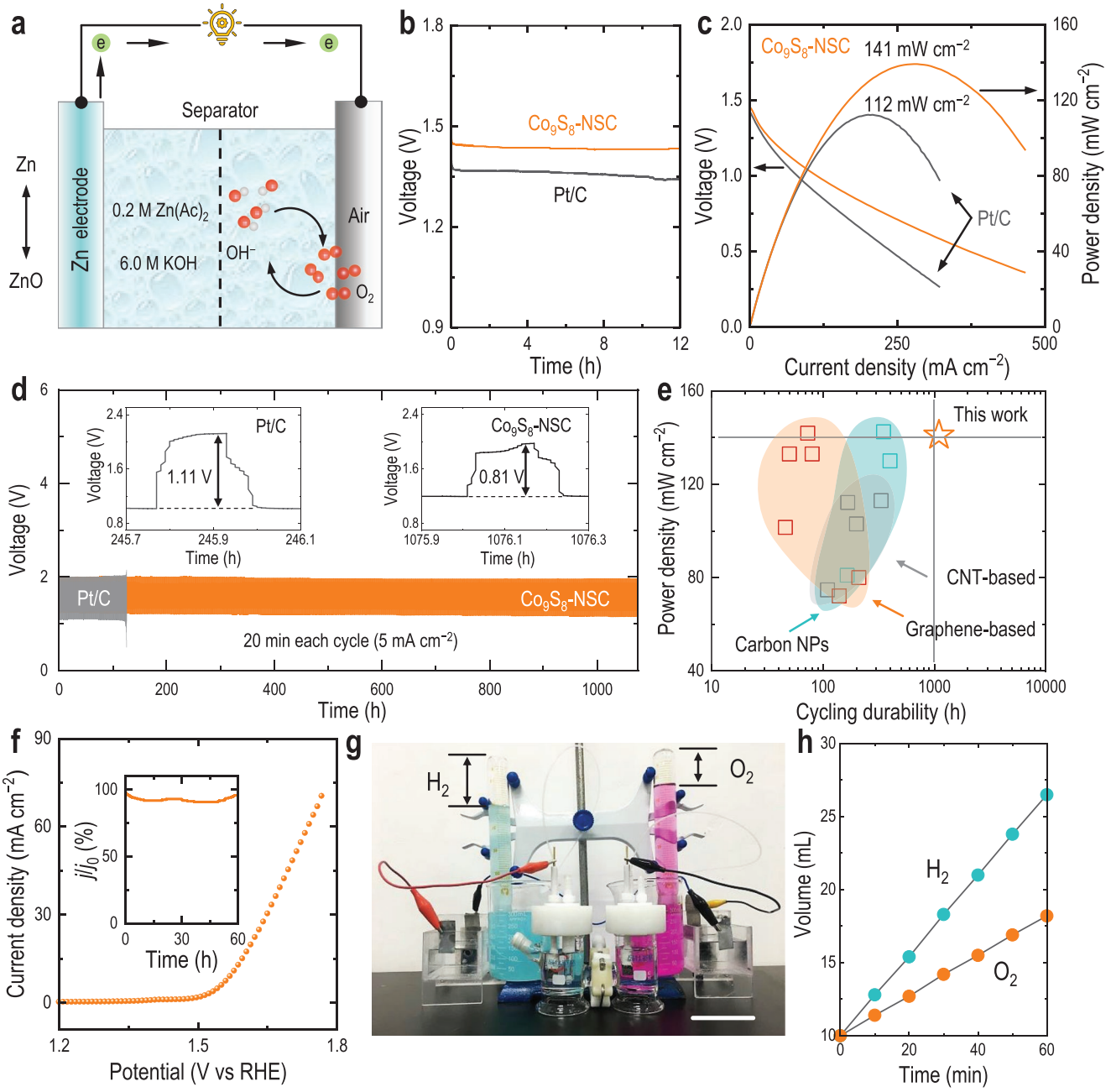

Figure 4. Liquid ZAB and water splitting. a) Schematic of ZAB using a mixed electrolyte (6.0 M KOH + 0.2 M zinc acetate ($Zn(Ac)_2$)). b,c) Open-circuit plots b), and discharge polarization curves and power densities of Co_9S_8-NSC and Pt/C catalyst. d) Galvanostatic charge–discharge cycling curves of Co_9S_8-NSC- and Pt/C-based ZABs (5 mA cm^{-2}). e) Performance comparison of ZABs using Co_9S_8-NSC and literature Co_9S_8-based catalysts loaded on different carbon materials. See Table S5 (Supporting Information) for more details. f) Polarization curve and stability test (inset; measured at 1.57 V) of the water splitting system based on Co_9S_8-NSC. g) Photograph of a water splitting system powered by ZAB using Co_9S_8-NSC. Scale bar is 5 cm. h) Volumes of O_2 and H_2 generated during the ZAB-powered water splitting process.

Specifically, a higher specific capacity of 779.7 mAh g^{-1} was achieved at 10 mA cm^{-2} than that achieved by the Pt/C catalyst (688.1 mAh g^{-1}) (Figure S29b, Supporting Information). Notably, the assembled ZAB using Co_9S_8-NSC displayed long-term charge-discharge cycling stability for up to 1077 h (i.e., > 3200 cycles), while the voltage gap was maintained at ≈0.80 V (Figure 4d). The Co_9S_8-NSC-based ZAB catalyst outperformed most previously reported Co_9S_8 catalysts loaded onto different carbon materials (e.g., carbon NPs, graphene-based, and CNT-based support materials; Table S5, Supporting Information), in terms of the extended cycling durability (i.e., 2–20 times longer) and the large power density (> 140 mW cm^{-2}) (Figure 4e), which is likely due to the electrochemical stability of the micro/mesoporous pLF support over repeated use (Figure S30, Supporting Information), as well as the superhydrophilicity that is helpful for efficient mass transfer[67] (Figure S31,

Supporting Information). The practical applicability was also further evaluated using two integrated ZABs that can power small fans and light bulbs (Figure S32, Supporting Information), demonstrating the real-world use of these catalysts.

2.8. Water Splitting by Co_9S_8-NSC

The potential application of Co_9S_8-NSC in water splitting was first examined by a two-electrode setup. A potential of 1.57 V was achieved at a current density of 10 mA cm^{-2}, and the time independence of the current density curve over a long period (60 h) suggested that the catalyst had good electrochemical stability (i.e., anticorrosion) (Figure 4f). Interestingly, water splitting could be powered by its own Co_9S_8-NSC ZAB system (Figure 4g). The electrolyte was separated by a Nafion membrane, and the generated H_2 and O_2 were collected using the water drainage method in an H-type electrolytic cell.[64] Bubbles of H_2 and O_2 were observed on the woven Co_9S_8-NSC sheets (Figure S33, Supporting Information). The volumes of H_2 and O_2 generated agree with the theoretical values of the volume ratio of 2:1 between H_2 and O_2 (Figure 4h), indicating a ≈100% Faradic yield.[68] In addition, the contact angle of H_2 was determined to be ≈150° on the woven catalyst immersed in 1 M KOH solution, indicating the super H_2-phobicity of the catalyst, which is conducive for the removal of the generated H_2 from the catalyst surface and consequently the continuous production of H_2.

2.9. Flexible Co_9S_8-NSC-Based Electronics

We further examined the flexibility of engineered Co_9S_8-NSC and its potential for wearable electronics. Owing to the robust long LFs and their entanglement, a woven LF mat could retain its integrity even after pyrolysis—the woven Co_9S_8-NSC mat (≈6 cm in diameter) could endure repeated folding-unfolding (**Figure 5**a), rolling-flattening (Figure 5b), and/or crumpling–smoothing (Figure S34, Supporting Information) treatments without losing its mechanical strength. Specifically, a single pyrolyzed pLF could hold the entire fiber mat (≈25 mg) and endure air blowing at a speed of ≈1–10 m s^{-1} (Movie S1, Supporting Information). To make full use of the sustained flexibility and mechanical strength of the composite catalyst, a flexible solid-state ZAB was constructed using the weavable catalyst Co_9S_8-NSC as the cathode and poly(vinyl alcohol)/KOH gel as the solid electrolyte. An open-circuit voltage of 1.40 V was attained, which remained largely unchanged upon folding (e.g., at 90° or 180°) (Figure S35, Supporting Information). In addition, the flexible solid-state ZAB device presented stable charge-discharge cycling profiles at different bending angles (e.g., 0–180°) for over 24 h (Figure 5c), where a high peak power density of 93.2 mW cm^{-3} was achieved during the full discharging process (Figure 5d). Furthermore, two flexible ZABs connected in series could be integrated to continuously supply the required power for a light bulb (rated voltage and power are 3 V and 0.06 W, respectively) (Figure 5e) or a mini fan (rated voltage of 3 V) (Figure 5f). Finally, the flexible ZAB device (two 1 × 3 cm^2 single-cell flexible batteries integrated into a fabric in series) could be wrapped on the wrist and provide stable power to a bracelet for health monitoring during daily activities (Figure 5g). These results demonstrate the flexibility and applicability of the Co_9S_8-NSC-based ZABs as promising materials for portable and wearable electronics. Informed written consent was obtained from the human participant for experimental testing of the wearables. In this case no ethical approval was required from any board/committee from Shuaijun Pan at Hunan University.

3. Conclusions

We demonstrated that naturally abundant and flexible LFs could serve as robust and promising supports for anchoring diverse nanomaterials (owing to their abundant reducible functional groups, such as hydroxyl and phenolic groups, and space confinement) and high-performance electrocatalysts after pyrolysis (owing to the mesoporous and conductive carbon matrix and the different electronic structure obtained upon doping of heteroatoms). During pyrolysis, high-entropy alloys and catalyst NPs were durably anchored by strong metal-support interactions while a mesoporous structure developed in the LFs (owing to the elimination of these reducible groups), enabling both high catalytic activity and sustained stability of the engineered electrocatalyst. The biomass-derived Co_9S_8 electrocatalyst exhibited three high-performance electrochemical functions (i.e., HER, OER, and ORR), featuring low overpotentials for HER (172 mV) and OER (276 mV) at a current density of 10 mA cm^{-2}, a high half-wave potential for ORR (0.87 V), and low Tafel slopes for ORR (72.5 mV dec^{-2}), HER (85.0 mV dec^{-2}), and OER (85.5 mV dec^{-2}). These functions were highly stable (i.e., > 91% retention) at a current density of 10 mA cm^{-2} for over 30 h as opposed to the decreasing performance displayed by commercial benchmarks (Pt/C and RuO_2; < 79% retention) under the same condition. Diverse applications were demonstrated using the nanoengineered electrocatalyst, including ZABs (liquid or flexible solid state), water splitting, and flexible electronics. Specifically, the assembled liquid ZAB, using a woven mat as the gas diffusion electrode (i.e., adhesive-free) that contained pLF and Co_9S_8 NPs, displayed a significantly extended charge-discharge cycling durability for up to 1077 h, which is ≈nine times longer than that displayed by commercial counterpart Pt/C. In addition, the flexibility of these naturally derived catalysts allows them to be woven/engineered into desired shapes and sizes. More importantly, they can be used in bulk without adhesive bonding while allowing for fast electrolyte transport through the macropores or along the conductive fibers as well as for the effective diffusion of gases generated (i.e., gas transport layer). This study provides a framework for the manufacturing of next-generation advanced materials for energy and storage applications from renewable biomass (such as wood cellulose[7]).

Supporting Information

Supporting Information is available from the Wiley Online Library or from the author.

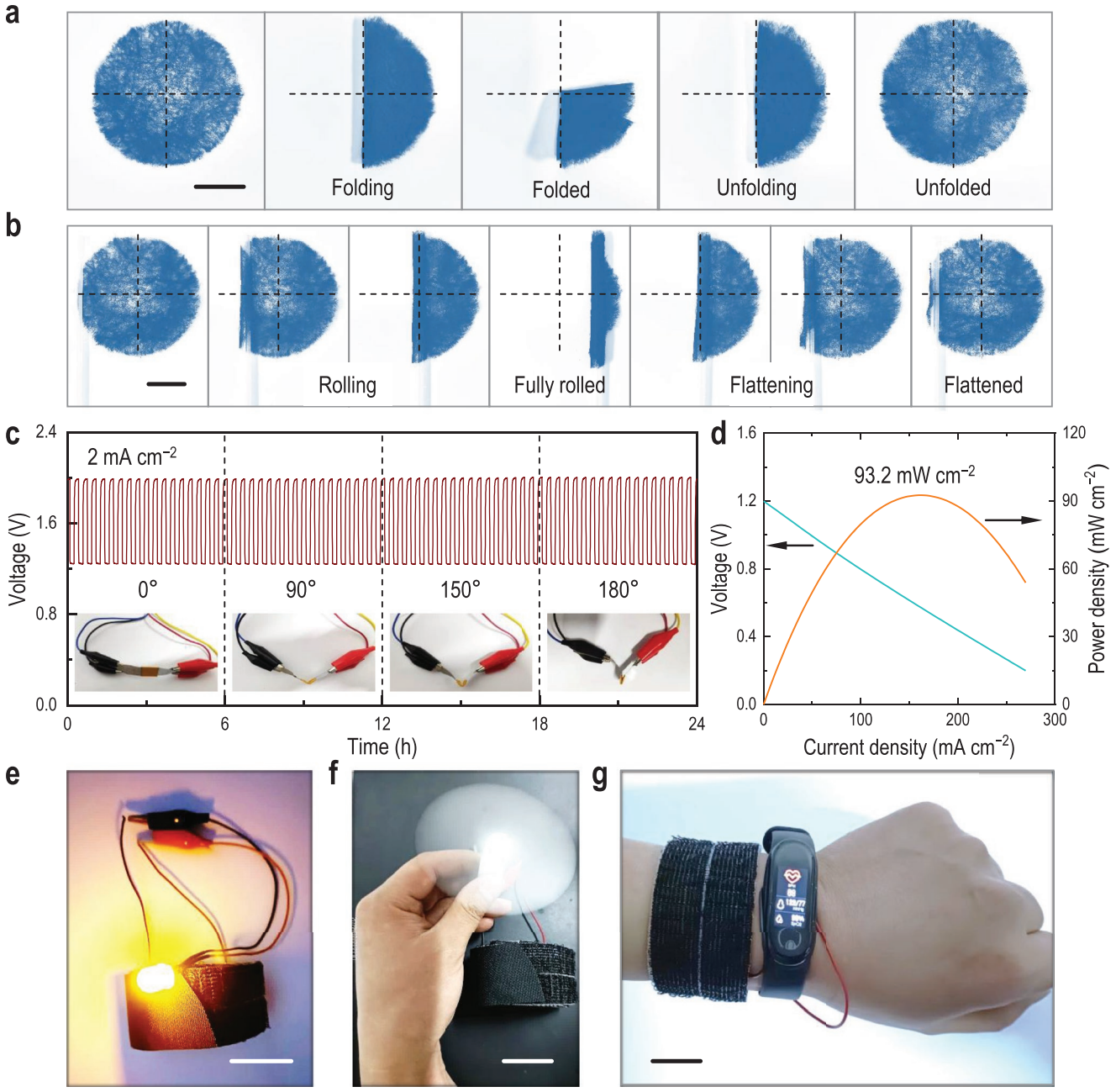

Figure 5. Flexible woven catalysts and solid-state ZAB assemblies. a,b) Folding and unfolding a), and rolling and flattening b) of the flexible woven catalyst. Scale bars are 2 cm. c) Cycling stability of solid-state ZAB at different bending angles (10 min charging and 10 min discharging). d) Discharge polarization curves and corresponding power density of solid-state ZAB. e–g) Photographs of the flexible woven catalyst (1×3 cm^2) incorporated into a wristband fabric supplying power to a bulb e), a mini fan f), and a smart watch g). Scale bars are 2 cm.

Acknowledgements

Z.L., X.W., and R.G. contributed equally to this work. This research was supported by the China Fundamental Research Funds for the Central Universities of China (S.P., Project nos. 021400–531118010741 and 021400–521119200134), National Natural Science Foundation of China (S.P., Grant no. 51703056), China Hunan Provincial Science and Technology Department (S.P., Project no. 2018JJ3028), China Changsha Science and Technology Bureau (S.P., Project no. kq2208015), China Scholarship Council (R.G., File no. 201606130022), China Petroleum and Chemical Corporation (W.X., Grant nos. 219012–3 and 420071–3), the SAXS/WAXS beamline and the X-ray absorption spectroscopy beamlime of the Australian Synchrotron, part of ANSTO (S.P., Project nos. 17146 and 18766), Australian National Health and Medical Research Council Senior Principal Research Fellowship (F.C., Grant no. GNT1135806), and Japan Society for the Promotion of Science (J.J.R, Fellowship no. P20373). R. G. acknowledges the Department of Chemical Engineering at the University of Melbourne for supporting her exchange studies. J.J.R. is recipient of an Australian Research Council Future Fellowship (Project no. FT210100669).

Open access publishing facilitated by The University of Melbourne, as part of the Wiley - The University of Melbourne agreement via the Council of Australian University Librarians.

Conflict of Interest

The authors declare no conflict of interest.

Data Availability Statement

The data that support the findings of this study are available from the corresponding author upon reasonable request.

Keywords

electrochemistry, flexible electronics, supported catalysts, surface engineering, triple-functional electrocatalysts

Received: October 6, 2022
Revised: November 27, 2022
Published online:

[1] Z. Li, C. Chen, H. Xie, Y. Yao, X. Zhang, A. Brozena, J. Li, Y. Ding, X. Zhao, M. Hong, H. Qiao, L. M. Smith, X. Pan, R. Briber, L. Hu, *Nat. Sustainability* **2022**, *5*, 235.
[2] C. Cao, Z. Lin, X. Liu, Y. Jia, E. Saiz, S. E. Wolf, H. D. Wagner, L. Jiang, Q. Cheng, *Adv. Funct. Mater.* **2021**, *31*, 2102923.
[3] W. Choi, D. Heo, T. Kim, S. Jung, M. Choi, J. Heo, J.-S. Kwon, B.-S. Kim, W. Lee, W.-G. Koh, J. H. Cho, S. Lee, J. Hong, *Adv. Sci.* **2022**, *9*, 2105420.
[4] G. Yao, D. Jiang, J. Li, L. Kang, S. Chen, Y. Long, Y. Wang, P. Huang, Y. Lin, W. Cai, X. Wang, *ACS Nano* **2019**, *13*, 12345.
[5] X. He, C. Fan, T. Xu, X. Zhang, *Nano Lett.* **2021**, *21*, 8880.
[6] K. Ariga, D. Leong, T. Mori, *Adv. Funct. Mater.* **2017**, *28*, 1702905.
[7] C. Yang, Q. Wu, W. Xie, X. Zhang, A. Brozena, J. Zheng, /araga, B. H. Ko, Y. Mao, S. He, Y. Gao, P. Wang, M. Tyagi, F. Jiao, R. Briber, P. Albertus, C. Wang, S. Greenbaum, Y.-Y. Hu, A. M. Isogai, K. Xu, Y. Qi, L. Hu, *Nature* **2021**, *598*, 590.
[8] J. N. Tiwari, N. K. Dang, S. Sultan, P. Thangavel, H. Y. Jeong, K. S. Kim, *Nat. Sustainability* **2020**, *3*, 556.
[9] P. Peng, L. Shi, F. Huo, C. Mi, X. Wu, S. Zhang, Z. Xiang, *Sci. Adv.* **2019**, *5*, eaaw2322.
[10] M. Ledendecer, S. Calderon, C. Papp, H. Steinruck, M. Antonietti, M. Shalom, *Angew. Chem., Int. Ed.* **2015**, *54*, 12361.
[11] H.-F. Wang, C. Tang, B. Wang, B.-Q. Li, Q. Zhang, *Adv. Mater.* **2017**, *29*, 1702327.
[12] J. C. Matsubu, S. Zhang, L. DeRita, N. S. Marinkovic, J. G. G. Chen, W. Graham, X. Pan, P. Christopher, *Nat. Chem.* **2017**, *9*, 120.
[13] S. Xu, Y. Yao, Y. Guo, X. Zeng, S. D. Lacey, H. Song, C. Chen, Y. Li, J. Dai, Y. Wang, Y. Chen, B. Liu, K. Fu, K. Amine, J. Lu, L. Hu, *Adv. Mater.* **2017**, *30*, 1704907.
[14] G. Nie, X. Zhao, J. Jiang, Y. Luan, J. Shi, J. Liu, Z. Kou, J. Wang, Y. Z. Long, *Chem. Eng. J.* **2020**, *402*, 126294.
[15] S. J. Tauster, S. C. Fung, R. L. Garten, *J. Am. Chem. Soc.* **1978**, *100*, 170.
[16] T. W. van Deelen, C. Hernández Mejía, K. P. de Jong, *Nat. Catal.* **2019**, *2*, 955.
[17] J. Zhang, Y. Zhao, C. Chen, Y.-C. Huang, C.-L. Dong, C.-J. Chen, R.-S. Liu, C. Wang, K. Yan, Y. Li, G. Wang, *J. Am. Chem. Soc.* **2019**, *141*, 20118.
[18] J. Zhang, H. Yang, B. Liu, *Adv. Energy Mater.* **2021**, *11*, 2002473.
[19] X. Li, H. Rong, J. Zhang, D. Wang, Y. Li, *Nano Res.* **2020**, *13*, 1842.
[20] Y.-N. Gong, L. Jiao, Y. Qian, C.-Y. Pan, L. Zheng, X. Cai, B. Liu, S.-H. Yu, H.-L. Jiang, *Angew. Chem., Int. Ed.* **2020**, *132*, 2727.
[21] B. Han, Y. Guo, Y. Huang, W. Xi, J. Xu, J. Luo, H. Qi, Y. Ren, X. Liu, B. Qiao, T. Zhang, *Angew. Chem., Int. Ed.* **2020**, *59*, 11824.
[22] Y. Pan, R. Lin, Y. Chen, S. Liu, W. Zhu, X. Cao, W. Chen, K. Wu, W.-C. Cheong, Y. Wang, L. Zheng, J. Luo, Y. Lin, Y. Liu, C. Liu, J. Li, Q. Lu, X. Chen, D. Wang, Q. Peng, C. Chen, Y. Li, *J. Am. Chem. Soc.* **2018**, *140*, 4218.
[23] W. Liu, L. Zhang, W. Yan, X. Liu, X. Yang, S. Miao, W. Wang, A. Wang, T. Zhang, *Chem. Sci.* **2016**, *7*, 5758.
[24] S. Zhou, L. Shang, Y. Zhao, R. Shi, G. I. N. Waterhouse, Y.-C. Huang, L. Zheng, T. Zhang, *Adv. Mater.* **2019**, *31*, 1900509.
[25] A. Han, B. Wang, A. Kumar, Y. Qin, J. Jin, X. Wang, C. Yang, B. Dong, Y. Jia, J. Liu, X. Sun, *Small Methods* **2019**, *3*, 1800471.
[26] A. Aijaz, J. Masa, C. Rçsler, W. Xia, P. Weide, A. R. Botz, R. Fischer, W. Schuhmann, M. Muhler, *Chem. Eur. J.* **2017**, *23*, 12125.
[27] N. Logeshwaran, I. Panneerselvam, S. Ramakrishnan, R. Kumar, A. Kim, D. Yoo, *Adv. Sci.* **2022**, *9*, 2105344.
[28] C. Li, M. Wu, R. Liu, *Appl. Catal., B* **2019**, *244*, 150.
[29] T. Guo, K. Wang, G. Zhang, X. Wu, *Appl. Surf. Sci.* **2019**, *469*, 331.
[30] B. Hang, N. Li, W.-J. Ong, N. Zhou, *J. Mater. Chem. A* **2019**, *7*, 27620.
[31] H. Bao, Y. Qiu, X. Peng, J.-A. Wang, Y. Mi, S. Zhao, X. Liu, Y. Liu, R. Cao, L. Zhuo, J. Ren, J. Sun, J. Luo, X. Sun, *Nat. Commun.* **2021**, *12*, 238.
[32] S. Zhou, Y. Zhao, R. Shi, Y. Wang, A. Ashok, F. Héraly, T. Zhang, J. Yuan, *Adv. Mater.* **2022**, *34*, 2204388.
[33] Q. Wang, J. Cai, G. Biesold-McGee, J. Huang, Y. Ng, H. Sun, J. Wang, Y. Lai, Z. Lin, *Nano Ener.* **2020**, *78*, 105313.
[34] M. Wu, H. Shuai, Q. Cheng, L. Jiang, *Angew. Chem., Int. Ed.* **2014**, *53*, 3358.
[35] Y. Zhang, Z. Guo, *Chem. Lett.* **2014**, *43*, 1137.
[36] S. Pan, E. Goudeli, J. Chen, Z. Lin, Q.-Z. Zhong, W. Zhang, H. Yu, R. Guo, J. J. Richardson, F. Caruso, *Angew. Chem., Int. Ed.* **2021**, *60*, 14586.
[37] F. Xu, J. Zhao, J. Wang, T. Guan, K. Li, *J. Colloid Interface Sci.* **2022**, *608*, 2623.
[38] Y. Gong, G. Han, Y. Zhang, J. Zhang, W. Jiang, Y. Pan, *Polym. Degrad. Stab.* **2015**, *118*, 104.
[39] J. J. Richardson, K. Liang, *Small* **2018**, *14*, 1702958.
[40] X. Wang, Y. Zhang, H. Si, Q. Zhang, J. Wu, L. Gao, X. Wei, Y. Sun, Q. Liao, Z. Zhang, K. Ammarah, L. Gu, Z. Kang, Y. Zhang, *J. Am. Chem. Soc.* **2020**, *142*, 4298.
[41] D. Lyu, S. Yao, A. Ali, Z. Tian, P. Tsiakaras, P. Shen, *Adv. Energy Mater.* **2021**, *11*, 2101249.
[42] S. Chen, A. M. Abdel-Mageed, D. Li, J. Bansmann, S. Cisneros, J. Biskupek, W. Huang, R. J. Behm, *Angew. Chem., Int. Ed.* **2019**, *58*, 10732.
[43] J. Wang, H. Liu, Y. Liu, W. Wang, Q. Sun, X. Wang, X. Zhao, H. Hu, M. Wu, *Carbon* **2019**, *144*, 259.
[44] Z. Liu, Q. Zhou, B. Zhao, S. Li, Y. Xiong, W. Xu, *Fuel* **2020**, *280*, 118567.
[45] X. Zhu, J. Dai, L. Li, D. Zhao, Z. Wu, Z. Tang, L. Ma, S. Chen, *Carbon* **2020**, *160*, 133.
[46] M. Han, M. Shi, J. Wang, C. Yan, J. Jiang, S. Guo, Z. Sun, Z. Guo, *Carbon* **2019**, *153*, 575.
[47] I. S. Amiinu, Z. Pu, D. He, H. G. R. Monestel, S. Mu, *Carbon* **2018**, *137*, 274.
[48] S. Pan, R. Guo, M. Björnmalm, J. J. Richardson, L. Li, C. Peng, N. Bertleff-Zieschang, W. Xu, J. Jiang, F. Caruso, *Nat. Mater.* **2018**, *17*, 1040.
[49] S. M. Alshehri, J. Ahmed, A. Khan, M. Naushad, T. Ahamad, *ChemElectroChem* **2018**, *5*, 355.

[50] M. Zheng, Y. Ding, L. Yu, X. Du, Y. Zhao, *Adv. Funct. Mater.* **2017**, *27*, 1605846.
[51] A. Douka, Y. Xu, H. Yang, S. Zaman, Y. Yan, H. Liu, M. Salam, B. Xia, *Adv. Mater.* **2020**, *32*, 2002170.
[52] R. A. Sidik, A. B. Anderson, *J. Phys. Chem. B* **2006**, *110*, 936.
[53] C.-L. Yang, L.-N. Wang, P. Yin, J. Liu, M.-X. Chen, Q.-Q. Yan, Z.-S. Wang, S.-L. Xu, S.-Q. Chu, C. Cui, H. Ju, J. Zhu, Y. Lin, J. Shui, H.-W. Liang, *Science* **2021**, *374*, 459.
[54] T.-W. Song, C. Xu, Z.-T. Sheng, H.-K. Yan, L. Tong, J. Liu, W.-J. Zeng, L.-J. Zuo, P. Yin, M. Zuo, S.-Q. Chu, P. Chen, H.-W. Liang, *Nat. Commun.* **2022**, *13*, 6521.
[55] Z. Wang, Z. Lin, J. Deng, S. Shen, F. Meng, J. Zhang, Q. Zhang, W. Zhong, L. Gu, *Adv. Energy Mater.* **2020**, *11*, 2003023.
[56] Y. Jiao, Y. Zheng, K. Davey, S. Z. Qiao, *Nat. Energy* **2016**, *1*, 16130.
[57] Z. Zhang, X. Zhao, S. Xi, L. Zhang, Z. Chen, Z. Zeng, M. Huang, H. Yang, B. Liu, S. J. Pennycook, P. Chen, *Adv. Energy Mater.* **2020**, *10*, 2002896.
[58] H. Lu, W. Fan, Y. Huang, T. Liu, *Nano Res.* **2018**, *11*, 1274.
[59] S. Chen, L. Zhao, J. Ma, Y. Wang, L. Dai, J. Zhang, *Nano Energy* **2019**, *60*, 536.
[60] C. Wu, Y. Zhang, D. Dong, H. Xie, J. Li, *Nanoscale* **2017**, *9*, 12432.
[61] H. Liu, J. Guan, S. Yang, Y. Yu, R. Shao, Z. Zhang, M. Dou, F. Wang, Q. Xu, *Adv. Mater.* **2020**, *32*, 2003649.
[62] S. Shi, Q. Liu, Y. Ma, Z. Fang, Z. Liang, G. Shao, B. Tang, W. Yang, L. Qin, X. Fang, *Adv. Energy Mater.* **2020**, *10*, 1903854.
[63] M. A. Ahsan, A. R. Puente Santiago, Y. Hong, N. Zhang, M. Cano, E. Rodriguez-Castellon, L. Echegoyen, S. T. Sreenivasan, J. C. Noveron, *J. Am. Chem. Soc.* **2020**, *142*, 14688.
[64] G. Zhou, G. Liu, X. Liu, Q. Yu, H. Mao, Z. Xiao, L. Wang, *Adv. Funct. Mater.* **2021**, *32*, 2107608.
[65] K. Wu, L. Zhang, Y. Yuan, L. Zhong, Z. Chen, X. Chi, H. Lu, Z. Chen, R. Zou, T. Li, C. Jiang, Y. Chen, X. Peng, J. Lu, *Adv. Mater.* **2020**, *32*, 2002292.
[66] W. Peng, Y. Wang, X. Yang, L. Mao, J. Jin, S. Yang, K. Fu, G. Li, *Appl. Catal. B* **2020**, *268*, 118437.
[67] B. Q. Li, S. Y. Zhang, B. Wang, Z. J. Xia, C. Tang, Q. Zhang, *Energy Environ. Sci.* **2018**, *11*, 1723.
[68] Y. Gao, Z. Chen, Y. Zhao, W. Yu, X. Jiang, M. He, Z. Li, T. Ma, Z. Wu, L. Wang, *Appl. Catal., B* **2022**, *303*, 120879.